ScienceDirect®

Case Report

Effect of copper nanoparticle volume fraction on flow in a 3D lid-driven cavity with phase change materials using molecular dynamics simulation

Narinderjit Singh Sawaran Singh [a], Waqed H. Hassan [b c], Rifqa F. Thiab [d], Younis Mohamed Atiah Al-zahy [e], Soheil Salahshour [f g h], M. Hekmatifar [i]

Show more ⌄

≔ Outline | ⊲ Share ⟩⟩ Cite

Abstract

Background

Phase Change Materials are substances characterized by specific properties, including defined melting points and substantial latent heat of fusion. Effective heat transfer management is vital in modern industries, as it supports essential processes across various sectors.
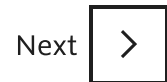
Methods

This study investigates the effect of copper nanoparticle volume fraction on flow behavior and thermal dynamics in a 3D lid-driven cavity. This enclosure was a controlled

environment filled with phase change materials, designed to optimize thermal energy management. The system configuration comprised a wavy bottom wall and an adaptable upper wall, allowing for dynamic adjustments during the simulation. The results show that as the volume ratio of copper nanoparticles increased from 1% to 3%, the steady heat transfer process in the simulated nanoparticles also increased. Increasing the volume ratio from 1% to 3% resulted in a decrease in the maximum density of nanoparticles, which decreased from 0.0152 to 0.0146 atom/$Å^3$. Additionally, this increase led to a rise in thermal conductivity from 1.26 to 1.45 W/m·K and in heat flux from 8.26 to 9.95 W/m^2.

Significant Findings

The study demonstrates that optimizing the volume fraction of Cu-NPs in PCMs can significantly enhance thermal conductivity and heat flux, offering potential improvements in thermal energy storage systems.

[< Previous]   [Next >]

Keywords

Phase change material; Density; Heat flux; Thermal conductivity; Molecular dynamics simulation

1. Introduction

Due to their variable and intermittent nature, renewable energies require a suitable method for optimal exploitation [1]. Therefore, thermal energy storage technology's importance becomes clearer [2,3]. This technology can improve the reliability and efficiency of renewable energy conversion systems [4]. Generally, thermal energy storage changes the material's internal energy in a tangible, latent, and thermochemical way or a combination [5,6]. Materials used in thermal storage systems, characterized by high latent heat, suitable phase change temperatures (Ts), and minimal volume change during phase transitions, are referred to as phase change materials (PCMs) [7]. The thermal performance of PCMs is crucial for effectively designing and optimizing thermal energy storage systems. PCMs can absorb and release substantial thermal energy during melting and freezing [8,9]. However, an axial transformation occurs as ambient T gradually decreases, resulting in a loss of stored latent heat. PCMs gradually change from liquid to solid phases [10,11]. This phase change is

characterized by the crystallization of material, effectively solidifying it. Various methods are currently employed to enhance the performance of thermal energy storage systems, including increasing heat transfer (HT) levels, using multiple PCMs simultaneously, microcoating PCMs, and adding nanostructured materials [12]. Meanwhile, with the advancement of nanotechnology, metal particles and metal oxides with nanoscale dimensions in PCMs were used to enhance the thermal properties of fluids [13,14]. The high specific surface area of nanoparticles (NPs) facilitates greater HT. Additionally, due to their unique properties, NPs significantly alter the thermophysical properties of materials they are mixed with [15]. Among metallic NPs, copper NPs (Cu-NPs) gained attention due to their anti-bacterial property, high TC, and low cost [16]. Cu is promising for replacing the expensive Ag as the thermally conductive particle, especially for large-scale applications [17]. Another advantage of Cu-NPs is that they oxidize, which can easily mix with polymers or macromolecules and are relatively stable in terms of both physical and chemical properties. Cu may also cause environmental hazards; thus, direct use of Cu and its compounds in higher doses should be restricted [18].

Researchers conducted various research in this field, some of which are mentioned. Huang et al. [19] utilized non-equilibrium molecular dynamics (NEMD) simulations to study how various graphene shapes interact with PCMs and influence thermal conductivity (TC). The results indicate that the orientation of various paraffin chains on non-covalently functionalized graphene surfaces indirectly affects TC. This effect results from the alignment of high-frequency vibrations with phonon vibrations, indicating that graphene oxide outperforms single-layer graphene as a superior thermal conductor. Harish et al. [20] researched the TC of lauric acid combined with graphene-NPs. Their study developed a phase change nanocomposite using lauric acid and chemically functionalized graphene nanoplatelets and measured its TC using the transient hot wire method. They found that adding 1% by volume of graphene resulted in a 230% increase in TC. Ghasemiasl et al. [21] performed a numerical analysis of phase change processes using finite element analysis. They modeled a rectangular capsule filled with a PCM and found that adding Al-NPs at a volume fraction (VF) of 0.2 decreased the melting time by 12.5%. In addition, they showed that when Cu-NPs at a VF of 0.2 were added to the PCM, the freezing time decreased by 18.8%. Huo et al. [22] explored HT enhancement in PCMs reinforced with NPs. They employed the multi-time network Boltzmann model for numerical analysis of phase change, examining the effects of NP position and VF. Their findings revealed that PCMs with NPs melted faster when a separate plate was positioned in the middle of the cavity. However, if the plate's position was less than 0.3 relative to the cavity, the melting process slowed due to heat accumulation near the plate. Chu et al. [23] investigated the freezing process using NPs in a unique approach. They combined primary PCMs with NPs and

considered waveforms for the walls. According to the obtained results, the expansion of the wave wall domain resulted in a 22.66% reduction in solidification time, indicating an improved solidification rate. Furthermore, incorporating NPs resulted in an approximately 17.9% increase in the discharge rate. Hekmatifar et al. [24] investigated the effect of Cu–NPs on Ar base fluid. Their study showed that Cu–NPs accelerated the phase transition process, decreasing the duration of the transition. Additionally, the inclusion of Cu–NPs improved the maximum density (Max-D) and TC of nanofluid. Garcia et al. [25] investigated the use of waste wood ash (WWA) in geopolymer concrete and concluded that WWA mainly serves as a filler, although it increases the compressive strength when used in moderate quantities. Their work underlined the contribution of industrial by-products to the enhancement of material properties and sustainable construction. Çelik et al. [26] explored the performance of concrete produced with partial substitution of fine and coarse aggregates by ground glass powder and crushed waste glass, respectively. Their results indicated that whereas glass powder improved strength by pozzolanic action, larger particles of glass introduce voids and thus decrease mechanical performance. They recommended 20% replacement for optimum strength and durability.

Prior works presented thermal characteristics of NP-enhanced PCMs by studying TC, phase transition dynamics, and enhancement in HT using methods like MD, finite element analysis, and numerical modeling. However, there was a gap in understanding the behavior of Cu–NPs in complex geometries. While previous studies explored the thermal properties of PCMs with NPs, this study was the first to employ MD simulations to investigate the effect of VF of Cu–NP in a 3D lid-driven cavity with a wavy bottom wall. It is worth mentioning that the MD method, a computational simulation technique widely used in scientific fields, particularly material science and nanotechnology, was employed for the first time in this study [27,28]. In this research, to investigate the thermal properties of the simulated structure's cell, various parameters, including Max-D, maximum velocity (Max-V), maximum temperature (Max-T), heat flux (HF), and TC, were affected by different VFs of Cu–NPs. By modeling a complex three-dimensional cavity with a wavy lower wall and a movable upper wall, the study employed advanced simulation techniques and realistic geometries to gain new insights into optimizing nanocomposites for enhanced thermal management. This approach addressed a significant gap by integrating detailed atomic-level observations with a dynamic model, providing a comprehensive understanding of how NP concentration affected thermal performance in practical applications.

2. Simulation and method

2.1. Simulation details

This study delved into the flow and thermal behavior of paraffin-PCMs incorporating Cu-NPs through MD simulations conducted over 20 ns. The primary objective was to address the low TC of the base paraffin-PCM by integrating Cu-NPs known to enhance thermal transport. Detailed molecular modeling was performed using Avogadro software to accurately represent the paraffin matrix, Cu-NPs, and the atomic-scale geometry of the simulation environment. The simulation was conducted in a properly designed three-dimensional atomic cavity, which comprised a wavy iron wall at the bottom for greater surface interactions. The upper boundary consisted of a movable wall to model dynamic thermal behavior, whereas the sidewalls were fixed and insulated against heat loss outside the system. This arrangement enabled the complete examination of the paraffin-Cu-NPs interactions, recording the influences of wall-induced thermal fluctuations and structural confinement on HT efficiency. A detailed schematic of the experimental setup is provided in Fig. 1 of a research paper, offering a comprehensive overview of the simulation configuration. The simulation box measured $80 \times 100 \times 100 Å^3$. Periodic boundary situations were applied exclusively in X, Y, and Z-directions. The employment of periodic boundaries made the domain seamless, providing a virtually infinite system with minimum edge effects that were useful to capture the phenomena of fluid and thermal fields. With this setup, a more accurate flow pattern representation and T-distribution were established since continuity of the fluid properties along the boundaries of the domain was allowed. The Nose-Hoover thermostat was selected for its ability to maintain a constant T during the simulation, which was crucial for accurately modeling the thermal behavior of PCMs [29]. The MD simulation employed a combination of force fields to effectively capture the system's interactions. The Embedded Atom Method (EAM) was employed to model metallic interactions between Cu-NPs to capture many-body effects that were critical to metallic bonding. The interactions of the van der Waals between the paraffin molecules and Cu-NPs were modeled by the Lennard-Jones (LJ) potential, considering appropriate dispersion forces with no-bond interactions. In addition, the Coulombic potential was utilized to account for electrostatic interactions within the system, which was particularly significant for simulating charge distributions in the paraffin matrix. Such a multiscale approach allowed for the accurate vision of atomic interaction processes and permitted the correct evaluation of the HT mechanisms in the presence of Cu-NPs. The NVT ensemble was applied as needed to ensure atomic arrangement stability, and the system's equilibrium was monitored by analyzing changes in kinetic energy (KE) and total energy (TE) of Cu-NPs. The validation of simulation settings and calculation methods was conducted after the system reached equilibrium to ensure the accuracy and reliability of observed results. Specifications of the simulated structure are given in Table 1.
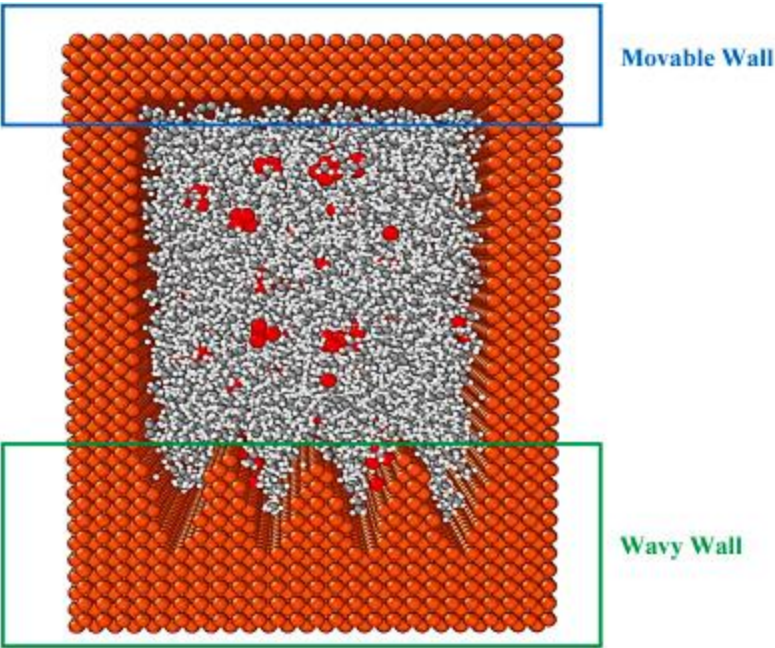
Download: Download high-res image (1MB)
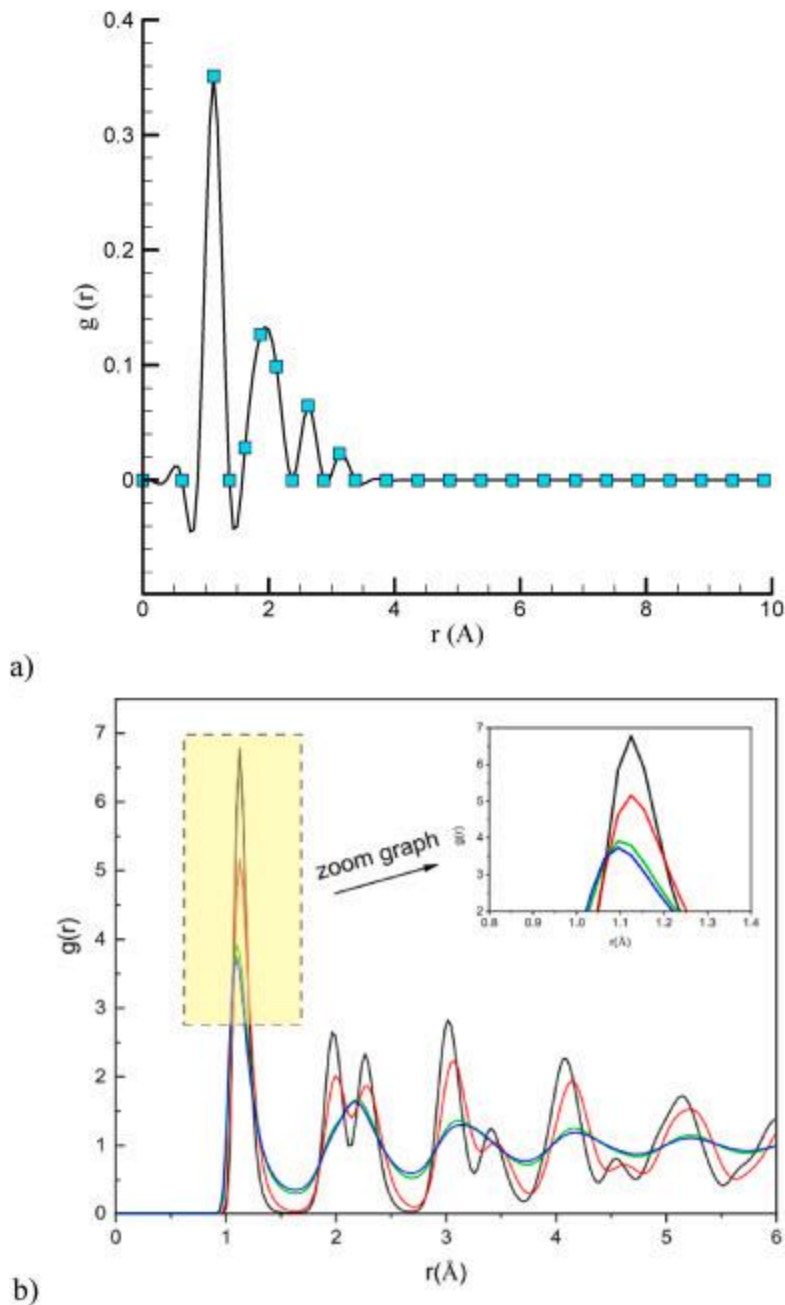Download: Download full-size image

Fig. 1. Schematic of the modeled structure in the present study.

Table 1. Specifications of the simulated structure.

Parameter	Value/Description
Simulation Box Dimensions	80Å×100Å×100Å
Boundary Conditions	Periodic in X, Y and Z-directions.
Simulation Duration	20 ns
Time Step	0.01 fs
Initial T	300K
Thermostat	Nose-Hoover
Software Used	LAMMPS, Avogadro, Packmol
T Damping	0.1
Equilibrium Monitoring	Changes in KE and TE

2.2. Validation of the computational method in the present study

The validity of the calculation method and simulation parameters was evaluated following the observation of the equilibrium in the simulated atomic structure. To achieve this objective, the radial distribution function (RDF) of the paraffin structure in the initial atomic sample was computed. The RDF denoted how particles were arranged within an atomic sample under specific conditions. Furthermore, this computational quantity's pattern functioned as an indicator of the phase of atomic structures. Consequently, it can be a valuable instrument for the identification of structures. Fig. 2 illustrates the RDF for the paraffin structure, which was consistent with previous structural reports for this sample. This confirmed the appropriateness of the calculation method and parameters employed in this research [30]. On the other hand, the atomic arrangement of the entire sample after achieving structural equilibrium further indicated the appropriateness of the calculation method in future research. The RDF results were compared with experimental data from Refs. [[30], [31], [32]], showing good agreement and confirming the accuracy of the simulation parameters.

a)

b)

Download: Download high-res image (402KB)

Download: Download full-size image

Fig. 2. Total RDF in paraffin sample after structure equilibration a T=300K for 10 ns b) the referenced article [33].

3. Results and discussion

3.1. The equilibration process

The equilibration process allows the system to reach a stable state. During this phase, the initial configuration, often generated randomly or from a theoretical model, may not reflect

the true thermodynamic state of the material. By allowing the system to equilibrate, you ensure that it accurately represents the physical conditions being studied. For this purpose, the changes in KE and TE are investigated during 10 ns. After 10 ns, KE converges to approximately 2100 eV. From a computational perspective, TE is the sum of kinetic and potential energy within the simulated NPs. Thus, changes in this parameter indicated structural stability. Notably, as shown in Fig. 3, TE gradually converges to −93470.50 eV over 10 ns. This convergence indicated equilibrium within simulated NPs, supporting the practical applicability of this atomic model in real-world scenarios.
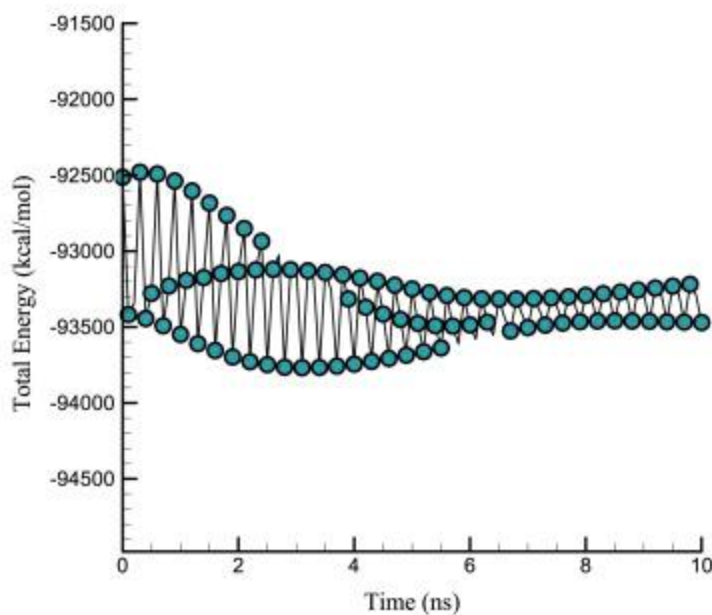
Download: Download high-res image (290KB)

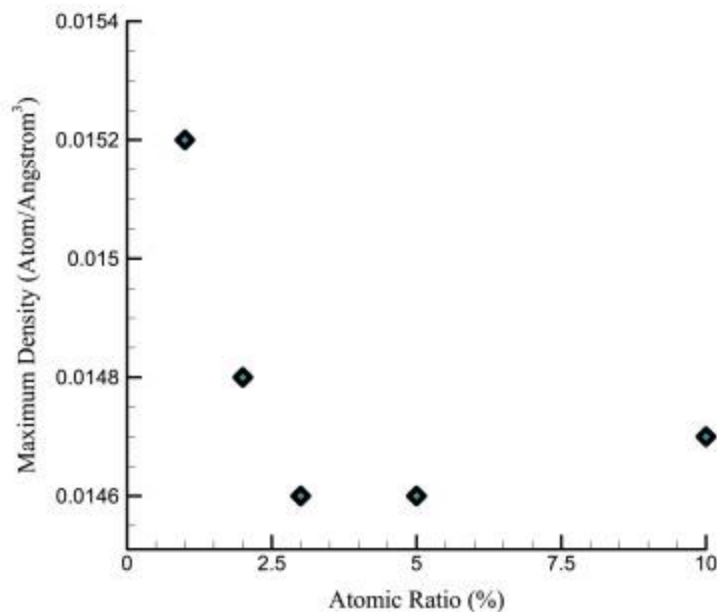Download: Download full-size image

Fig. 3. TE variations concerning simulation time in the structure equilibration stage at T=300K.

3.2. Effect of VF of Cu-NPs

Cu-NPs demonstrated optimal thermal behavior. Additionally, VF used in these structures was important, alongside the type of NPs. To investigate this issue, the VF of Cu-NPs was set at 1%, 2%, 3%, 5%, and 10%, and the simulations were repeated. The results indicate that all atomic structures simulated at this stage, with various VFs of NPs, exhibited thermodynamic stability and appropriate structure. The behavior of D, V, and T profiles followed the previous general pattern, with differences only in their values. A notable observation in Fig. 4 is the inverse relationship between Max-D and the concentration of Cu-NPs. The results show that Max-D decreases as the concentration of Cu-NPs increased.

At its lowest point, Max-D reaches to 0.0146 atom/Å^3 under the effect of Cu-NPs. This trend indicated that the presence of Cu-NPs altered atomic packing, leading to a lower Max-D. This disruption may happen because the NPs can bring some extra interstitial spaces or may disturb the arrangement of atoms and thereby reduce the atomic density as a whole. This reduces Max-D can enhance its ability to absorb more heat, as more space in the atomic structure may lead to better accommodation of thermal energy. This relation can be used practically to optimize using Cu-NPs in designing PCMs for thermal energy storage systems. By fine-tuning the concentration of Cu-NPs, a balance between density and TC may be achieved to improve the efficiency and effectiveness of energy storage systems.
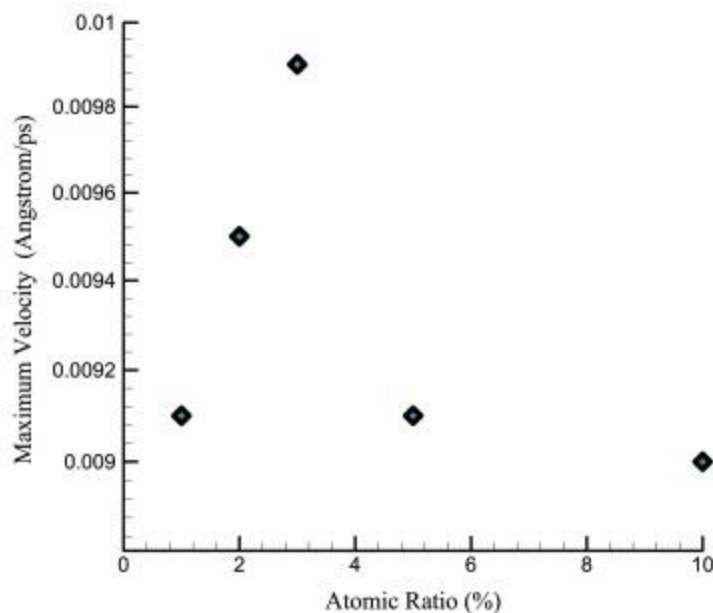

Download: Download high-res image (168KB)
Download: Download full-size image

Fig. 4. Max-D variations in simulated NPs in the presence of 3% Cu-NPs based on VF of NPs and after 10 ns.

Fig. 5 shows the variations in Max-V in simulated atomic samples with Cu-NPs, based on the VF of NPs, after 10 ns. The highest Max-V values occurred in the system with 3% Cu-NPs by volume. This finding had significant implications for the thermal behavior of the sample. The recorded Max-V was 0.0099Å/ps. It indicated that the presence of Cu-NPs in the system, with this particular amount, increased significantly the KE of the particles. This may be realized since the high Max-V represents a more energetic atomic movement reflecting, in fact, a better thermal response. Increasing KE in the system, led directly to the improvement of HT properties. The heat properties improved for this system due to the material having a greater facilitation toward effective movement of the thermal energy inside it. The

improved value of Max-V at 3% Cu-NPs further elucidates the role of NPs in enhancing better atomic interactions within the PCM, which led to a more efficient transfer of heat. Hence, the system with 3% Cu-NPs was more capable of absorbing and releasing thermal energy and was more suitable for applications requiring high TC and efficient heat storage. From an applied standpoint, such a result thus led to development conclusions that contributed towards higher effectiveness related to heat thermal energy storage applications. Because optimization of Cu-NP concentration helped improve HT characteristics, more efficient applications in energy storage were availed for these PCM materials. This most likely led to new thermal energy storage system designs that can work with much higher efficiency and reliability in their performances, both at energy retention and energy release.
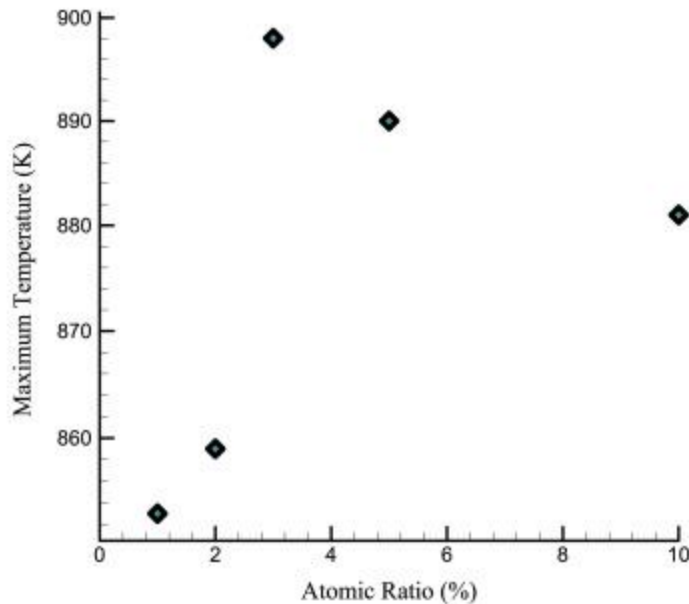

Download: Download high-res image (167KB)
Download: Download full-size image

Fig. 5. Max-V variations in simulated NPs in the presence of 3% Cu-NPs based on RV of NP's and after 10 ns.

Fig. 6 shows the variations in Max-T in simulated atomic samples with Cu-NPs, based on the VF of NPs, after 10 ns. As shown in Fig. 6, at a concentration of 3% Cu-NPs, the recorded Max-T was 898 K. This T rise itself signified the improvement in thermal stability and energy storage capacity of the system at this optimal concentration of NPs. Such a rise in T was most probably due to the enhanced efficiency of HT resulting from the uniform dispersion of Cu-NPs, which optimized the atomic interactions within the PCM matrix. However, a further increase in the concentration of NPs would result in clustering and disruption of the

atomic structure and the loss by the system of its capability to maintain or achieve better T stability. The optimal concentration can be interpreted from 3% Cu-NPs, where the NPs were adequately dispersed, which assisted in uniform heat distribution throughout the PCM. In such a concentration, the NPs cooperated with the PCM to increase the thermal capacity of the system without significant agglomeration or interference in the atomic structure. This balance was of critical importance because required dispersion-concentration made efficient conduction and storage of thermal energy possible.
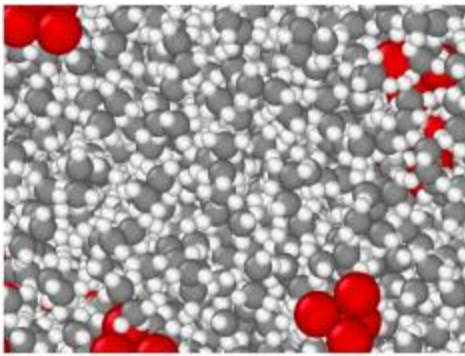

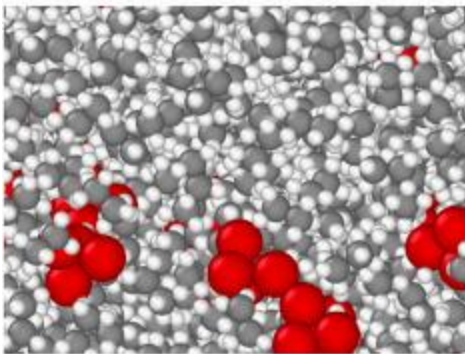Download: Download high-res image (153KB)
Download: Download full-size image

Fig. 6. Max-T variations in simulated NPs in the presence of 3% Cu-NPs based on the VF of NPs and after 10 ns.

In the following, the thermal behavior of simulated samples was investigated. The graphical output from MD simulations indicated thermodynamic equilibrium in all simulated samples. Fig. 7 shows the atomic arrangement of PCMs after 10 ns in the presence of Cu-NPs with VF of a) 1%, b) 2%, c) 3%, d) 4%, and e) 10%. These figures indicate that 10 ns was sufficient time to stabilize the system for HT. The final numerical results for the target structure at different VFs of NPs were obtained during this period. Ultimately, the structural outputs demonstrated balance and physical stability, as shown in Fig. 7.
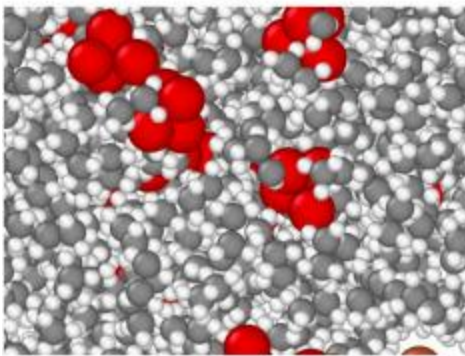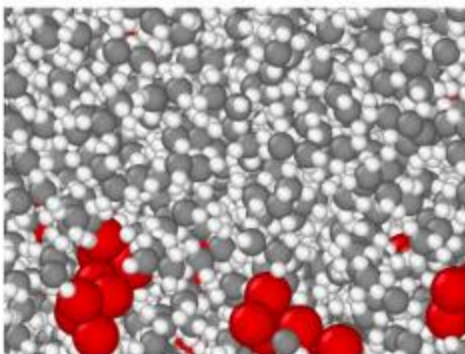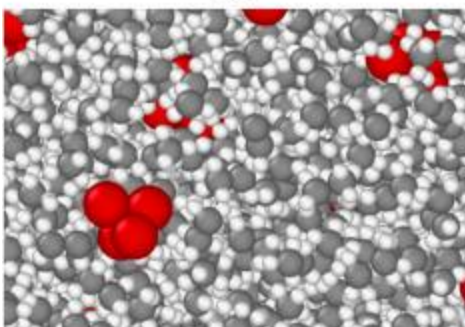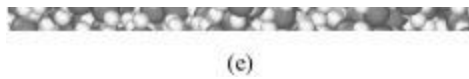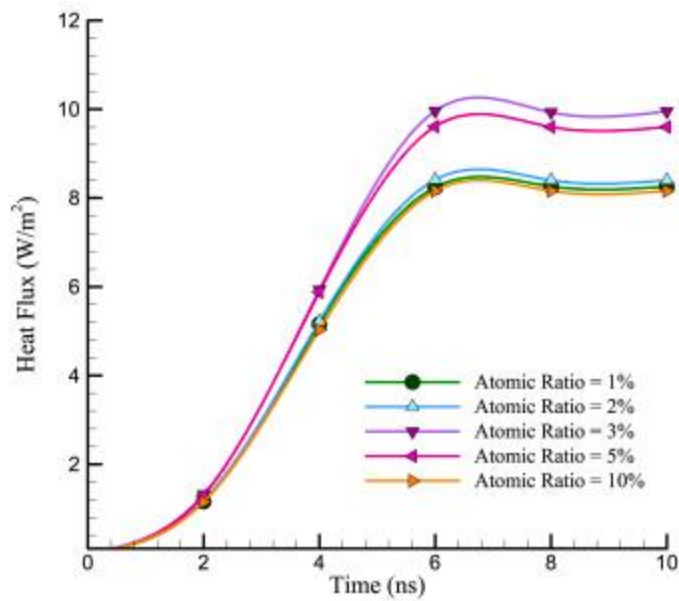
(a)

(b)

(c)

(d)

(e)

Download: Download high-res image (1MB)
Download: Download full-size image

Fig. 7. The atomic arrangement of the PCM after 10 ns in the presence of Cu-NPs with VF of a) 1, b) 2, c) 3, d) 4, and e) 10%.

The examination of HF and TC, as shown in Fig. 8, Fig. 9, follow a convincing pattern. Max-HT potential was evident in samples with 3% Cu-NPs. This phenomenon resulted from the formation of an optimal atomic HT chain. Such a well-ordered atomic chain only facilitated a more efficient flow of energy, greatly improving HF and TC when compared with other VFs. The increased concentration of Cu-NPs beyond 3% resulted in the clustering of NPs, hence disturbing the atomic alignment and thereby reducing thermal efficiency. This weakening effect manifested as a drop in HF and TC for the higher-concentration samples. This physically means that too many NPs, it led to agglomeration, creating a barrier to the paths of HT and hence making the system less capable of handling thermal energy efficiently. Fig. 8 shows the changes in HF in the simulated atomic samples with various VFs of Cu-NPs. The results indicate that the highest HF, recorded at 9.95, was obtained in the sample with 3% Cu-NPs. These findings were very important in the design of more efficient thermal energy storage systems since they pointed to the optimization of Cu-NP concentration to ensure the maximizing of thermal performance while foregoing inefficiencies brought about by excessive NP clustering.
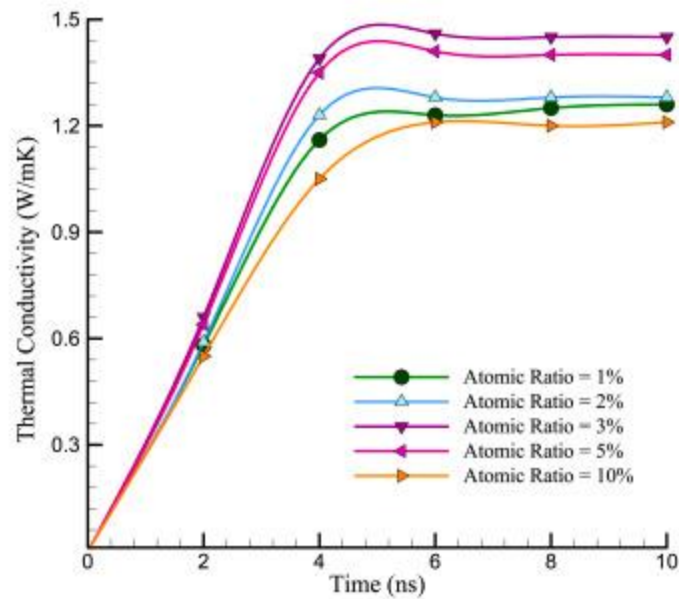
Fig. 8. HT variations in simulated atomic samples in the presence of Cu–NPs with different VF.

Fig. 9. TC variations in simulated atomic samples in the presence of Cu-NPs with different VF.

Fig. 9 shows the changes in TC in simulated atomic samples with various VF of Cu-NPs. The results indicate that TC peaks in the sample containing 3% Cu-NPs converge to a value of 1.45. This finding reinforced the concept of an optimal atomic HT chain in this configuration. This demonstrated that introducing Cu-NPs at this concentration enhanced the material's ability to conduct heat effectively. At this concentration, the Cu-NPs were well dispersed and interacted more efficiently with the surrounding PCM matrix for better enhancement of the overall TC of the system. Increasing the concentration beyond 3%, there was a noticeable decline in TC, suggesting that the system entered a regime where the Cu-NPs began to cluster. Also, as the VF increased, the NPs started aggregating and obstructing the normal distribution of atoms; hence, it decreased the efficiency in HT. Aggregation, therefore, caused local thermal resistance to the easy flow of heat through the system. On a physical basis, the explanation can be traced back to the atomic-scale interactions within the PCMs. At higher NP concentrations, the network of heat pathways became increasingly disjointed due to the clustering, thus impeding the material's ability to conduct heat efficiently. The results were bound to give enormous contribution to the design of more efficient thermal energy storage systems since they indicated the optimum concentration of Cu-NPs at which the enhancement of HT without losing the performance of a system by excessive clustering occurred. It helped in the selection of materials for higher thermal efficiency, important in optimizing energy storage and retrieval in practical applications. According to the previous study, it was depicted that the TC of PCMs in the presence of Cu NPs lies between 1 and 2 W/m.K [34]. Also, Wang et al. [35], showed that the addition of TiO_2 NPs to a paraffin wax matrix enhanced TC. More precisely, the TC of TiO_2/paraffin wax composites increased monotonically with TiO_2 loading up to 3 wt% and then remained constant or decreased slightly.

The selection of NP concentration had a substantial impact on the material's thermal characteristics in the larger framework of MD simulations. The atomic and thermal quantities found in this study for various Cu-NP concentrations after 10 ns are shown in Table 2. The quantitative changes in the Max-D, Max-V, Max-T, HF, and TC under various initial T values were summarized in this table. While Cu-NPs depict an optimum VF of 3% to improve TC and, consequently, the HF, other metallic or oxide-based NPs, such as Al_2O_3, TiO_2, or Ag may bring different properties due to their different TCs, specific heats, and interfacial interactions with the PCM matrix. For instance, Ag-NPs may enhance HT efficiency because of their higher TC, while oxide-based NPs, owing to their distinctive surface chemistry, could further cause stability modifications and phase transition changes.

In addition, the kind of used PCMs could have a considerable impact on thermal performance. A more polar PCM can cause stronger dispersion of NPs, which in turn reduces aggregations and retains more consistent thermal properties. On the other hand, nonpolar PCMs may undergo phase separation with reduced thermal efficiency at higher NP concentrations.

Table 2. Atomic and thermal quantities (Max-D in atom/Å^3, Max-V in Å/ps, Max-T in K, HF in W/m^2, TC in W/m.K) were obtained for various VFs of Cu-NPs after 10 ns.

VF of Cu-NPs (%)	Max-D (atom/Å^3)	Max-V (Å/ps)	Max-T (K)	HF (W/m^2)	TC (W/m.K)
1	0.0152 (±0.00003)	0.0091 (±0.00011)	853 (±4)	8.26 (±0.02)	1.26 (±0.03)
2	0.0148 (±0.00005)	0.0095 (±0.00017)	859 (±5)	8.40 (±0.01)	1.28 (±0.01)
3	0.0146 (±0.00002)	0.0099 (±0.00006)	898 (±4)	9.95 (±0.03)	1.45 (±0.01)
4	0.0146 (±0.00003)	0.0091 (±0.00008)	890 (±3)	9.60 (±0.01)	1.40 (±0.02)
10	0.0147 (±0.00005)	0.0090 (±0.00009)	881 (±5)	8.16 (±0.02)	1.21 (±0.01)

4. Conclusion

In this study, MD simulations were employed to investigate the atomic and thermal dynamics of PCMs containing Cu-NPs. The study began with an equilibration phase, allowing the NPs to achieve equilibrium in their atomic arrangement. Insights from this phase informed the analysis of how varying VF of Cu-NPs affects their thermal and dynamic properties. The results revealed that the system's energy converged to 2100 eV, and the TE stabilized at −93470.50 eV, indicating that equilibrium was reached within the NP structures. Increasing the VF of Cu-NPs from 1% to 3% resulted in a noticeable rise in TC from 1.26 to 1.45 W/m·K, and HF from 8.26 to 9.95 W/m^2. However, further increasing VF from 3% to 10% led to a decrease in both TC and HF, with TC dropping to 1.21 W/m·K and HF to 8.16 W/m^2. Max-V of NPs increased from 0.0091 to 0.0099 Å/ps when the VF increases from 1% to 3%, but then decreases to 0.0090 Å/ps at a VF of 10%. Meanwhile, Max-D decreases from 0.0152 to 0.0146 atom/Å^3 as VF increased from 1% to 3%, then increased to 0.0147 atom/Å^3 with a further increase to 10%. Increasing the VF from 1% to 3% raised Max-T from 853 K to 898 K. However, further increasing VF from 3% to 10% reduced Max-T to 881 K. These findings highlight the intricate relationship between the VF of Cu-NPs and the thermal and dynamic properties of the NP systems, demonstrating how variations in NP concentration affected their performance. While such atomic-scale simulation results were

useful, there was a limit to the direct applicability of findings to real macroscopic thermal management systems. MD simulations involved typical system sizes that were relatively small and were not able to represent the bulk behavior of a macroscopic system. Results also heavily depended on the choice of force fields, which modeled atomic interactions themselves but could hardly catch all the peculiarities of real materials, especially under extreme conditions. Besides this, in most MD simulations, periodic boundary conditions and idealized environments were considered that did not take into consideration the surface roughness, defects, or heterogeneity of real material. Other important environmental factors that were not thoroughly simulated included T gradients, fluid flow, and external pressures, as well as the geometries of macroscopic systems. Future studies could investigate the effects of hybrid NP systems or different PCMs on thermal performance, as well as the impact of more complex geometries on HT dynamics.

CRediT authorship contribution statement

Narinderjit Singh Sawaran Singh: Formal analysis, Data curation, Conceptualization, Writing – original draft. **Waqed H. Hassan:** Validation, Methodology, Writing – review & editing. **Rifqa F. Thiab:** Writing – original draft, Writing – review & editing. **Younis Mohamed Atiah Al-zahy:** Conceptualization, Methodology, Software. **Soheil Salahshour:** Writing – original draft, Writing – review & editing. **M. Hekmatifar:** Writing – original draft, Writing – review & editing.

Declaration of competing interest

The authors declare that they have no known competing financial interests or personal relationships that could have appeared to influence the work reported in this paper.

Appendix.

A. MD simulation

MD simulations are a highly accurate and powerful computational tool essential for studying atomic-scale interactions in materials. They bridge the gap among different time scales, connecting the microscopic world of atoms with macroscopic experiments and theoretical models. MD simulations model the interactions among atoms and molecules over time, providing valuable insights into material properties and tracking the physical movements of particles at atomic and molecular levels. This approach was particularly beneficial for complex molecular systems with many particles, where traditional analytical

techniques may be insufficient. MD simulations rely on numerically solving Newton's second law of motion, which describes the behavior of particles in dynamic, time-dependent situations [36]. The equation of motion is given by:

$$F_i = m_i a_i = -\nabla_i U = -\frac{dU}{dr_i} \qquad \text{(a-1)}$$

In Eq. a-1, F_i stands for external forces acting on the particles, U represents the potential energy of particles, m_i denotes the mass of individual particles, and r_i represents the positional coordinates of each particle. Velocity-Verlet algorithm is a widely used numerical method in MD simulations for accurately predicting particle motion over time. The algorithm begins by updating particle positions based on their current Vs and accelerations. This involves calculating the expected position of each particle at the next time step based on its current state of motion. After updating the positions, the algorithm calculates new accelerations for the particles, derived from the forces acting on them at these updated positions. Finally, it updates the velocities by averaging the accelerations at the beginning and end of the time step, ensuring that V reflects changes in acceleration. This approach is valued for its precision and stability, as it effectively conserves energy and maintains accuracy in tracking particle dynamics, making it particularly useful for simulations requiring detailed and reliable time evolution. This algorithm, which is widely used for tracking atom trajectories, relies on Taylor series expansions [[37], [38], [39]]:

$$r_i \ (t + \Delta t) = 2 \ r_i \ (t) - r_i \ (t - \Delta t) + \left(\frac{d^2 r_i}{dt^2}\right) \ (\Delta t)^2 \qquad \text{(a-2)}$$

$$v \ (t + \Delta t) = v \ (t) + \Delta t \ v \ (t) + \frac{\Delta t \ (a \ (t) + a(t + \Delta t))}{2} \qquad \text{(a-3)}$$

in Eq. a-3, 't' represents the time step. Eq. a-3 involves 'r,' which signifies the final position of particles in the system, and 'v,' representing the change in particle positions over time. The concept of TE is fundamental and crucial in MD simulations. TE refers to the sum of all bonding and non-bonding interactions affecting the particles in the system. It includes various energy contributions, such as:

Bonding Interactions: These involve covalent bonds among atoms, which contribute to the system's potential energy.

- *Non-bonding Interactions*: These include electrostatic interactions between charged particles and Van der Waals forces, which arise from transient dipole-induced dipole interactions and other non-covalent forces.

In MD simulation, TE is calculated to assess the system's stability and dynamics. This calculation helps assess the distribution of energy among different types of interactions and their contributions to the overall behavior of the system. Eq. a-4 governing this concept is provided for clarity [37].

$$E_{total} = E_{bonded} + E_{nonbonded} \tag{a-4}$$

In MD simulations, directly calculating the forces among a large number of particles is time-consuming and complex. To address these challenges, mathematical functions and potential models are used, as qualitative methods are impractical for such large systems. In this study, particle interactions were modeled using specific potential functions, such as LJ potentials, the EAM, and Coulombic potentials [[40], [41], [42], [43]]. LJ potential, as articulated in Eq. a-5, is a fundamental mathematical model used in MD simulations to describe the interactions between pairs of particles. This potential was essential for capturing the nuances of particle interactions in a simulated environment. It models both repulsive forces, which dominate when particles are very close, and attractive forces, which prevail at larger distances. Using LJ potential, researchers can precisely estimate the potential energy among interacting particles. This estimation was vital for analyzing particle behavior in various scenarios, such as predicting molecular arrangements, interactions, and responses to different environmental conditions. Thus, LJ potential provides a quantitative basis for studying molecular behavior and aids in understanding the physical properties and dynamics of simulated systems [44].

$$U_{LJ} = 4\varepsilon \left[\left(\frac{\sigma}{r} \right)^{12} - \left(\frac{\sigma}{r} \right)^{6} \right] r < r_c \tag{a-5}$$

Eq. a-5 introduces several key parameters for understanding molecular interactions in MD simulations. Within this, Eq.a-5 ε_{ij} denotes the depth of the potential well, σ_{ij} signifies the finite distance at which the potential function became zero, and r_{ij} represents the distance among particles. Additionally, r_c is the cut-off radius in the simulated samples, defining a critical distance beyond which interparticle interactions are considered negligible. While increasing computational accuracy and providing a precise description of interatomic interactions are essential in MD simulations, this can lead to reduced computational speed and longer simulation durations. As computing speed was limited by processor capabilities, researchers developed various approximations to accelerate calculations and reduce simulation times. Determining the values of ε_{ij} and σ_{ij} is a critical step in setting up an MD simulation. These values are usually obtained through empirical fitting to experimental data or quantum mechanical calculations. ε_{ij} represents the strength of intermolecular forces

while σ_{ij} defining the equilibrium distance at which these forces are in equilibrium.

$$\varepsilon_{ij} = \sqrt{\varepsilon_i \varepsilon_j} \tag{a-6}$$

$$\sigma_{ij} = \frac{\sigma_i + \sigma_j}{2} \tag{a-7}$$

The choice of ε_{ij} and σ_{ij} profoundly affected the accuracy and realism of MD simulations and enables the modeling of real interparticle interactions and the reproduction of experimental observations. These values are given in Table a-1.

Table a-1. LJ potential function parameters for the presented particles in the MD simulation [45,46].

Particle's type	ε (kcal/mol)	s (Å)
H	0.044	2.886
C	0.105	3.851
Cu	0.005	3.495
Fe	0.055	5.540

The non-bonded potential function within EAM played a pivotal role in defining the interactions among metal particles confined within the simulation box (SB). This function was particularly important for modeling interactions between particles that did not share direct chemical bonds. Unlike bond–based potential functions, the EAM approach incorporates embedding energy, which reflects how each atom's environment affected its energy, rather than relying solely on pairwise interactions. Mathematically, non-bonded interactions in EAM are described by Eq. a-8. This equation encapsulated the complex relationship between atoms by considering both pairwise potential energy and embedding energy, which was dependent on local atomic D. This dual approach allowed EAM to accurately simulate the behavior of metallic systems, where atoms interacted through a combination of direct and indirect effects, making it crucial for capturing the realistic properties of metals within simulation framework [47]:

$$U_i = F_\alpha \left(\sum_{i \neq j} \rho_\beta \left(r_{ij} \right) \right) + \frac{1}{2} \sum_{i \neq j} \phi_\beta \left(r_{ij} \right) \tag{a-8}$$

In Eq. a-8, ϕ_β is repulsive force, ρ_β is attractive force and r_{ij} represents the distance of particles from each other. Electric potential energy, specifically known as electrostatic potential energy (PE), is fundamentally important in particle interactions. This type of

potential energy arose from Coulomb's forces and was especially significant in systems containing electrically charged particles. Coulomb's law provides a foundational framework for understanding these electrostatic interactions. This law quantified the force between two point charges based on their magnitudes and the distance separating them. Thus, the arrangement of point charges within a system significantly affects overall electrostatic potential energy and the resultant forces acting on the charged particles. This critical relationship is expressed mathematically through Eq. a-9 [48].

$$U_{ij}(r) = \frac{-1}{4\pi\varepsilon_0} \frac{q_i q_j}{r_{ij}^2} \qquad\qquad (a\text{-}9)$$

Eq. a-9 introduces several key parameters q_j signifies the electric charge of particle j, q_i represents the electric charge of particle i, and r_{ij} denotes the distance separating these charges. Moreover, 'e' is a constant that stands for the electric permeability of free space. Numerically, the value of ε is precisely equal to $8.85 \times 10^{-12} \mathrm{F.\,m^{-1}}$. Eq.a-9 mathematically captures the relationship among electric charges, their separation distance, and the electric permeability of free space.

[Recommended articles]

Data availability

No data was used for the research described in the article.

References

[1]   W. Shepherd, D.W. Shepherd
        Energy Studies
        World Scientific Publishing Company (2014)
        Google Scholar ↗

[2]   H. Liu, X. Wang, D.J.S.E. Wu, Fuels
        Innovative design of microencapsulated phase change materials for thermal energy storage and versatile applications: a review
        3 (5) (2019), pp. 1091-1149
        Crossref ↗   View in Scopus ↗   Google Scholar ↗

[3]   S. Sami, S. Sadrameli, N.J.A.T.E. Etesami
        Thermal Properties Optimization of Microencapsulated a Renewable and Non-toxic Phase Change Material with a Polystyrene Shell for Thermal Energy Storage Systems, vol. 130 (2018),

pp. 1416-1424

[PDF] View PDF   View article   View in Scopus ↗   Google Scholar ↗

[4]   M.M. Umair, Y. Zhang, K. Iqbal, S. Zhang, B.J. A.e. Tang
"Novel strategies and supporting materials applied to shape-stabilize organic phase change materials for thermal energy storage
Rev., 235 (2019), pp. 846-873

[PDF] View PDF   View article   View in Scopus ↗   Google Scholar ↗

[5]   K. Muruganantham
Application of Phase Change Material in Buildings: Field Data vs. EnergyPlus Simulation
Arizona State University (2010)

Google Scholar ↗

[6]   A. Sharma, V.V. Tyagi, C.R. Chen, D.J.R. Buddhi, S.e. reviews
Review on thermal energy storage with phase change materials and applications
13 (2) (2009), pp. 318-345

[PDF] View PDF   View article   View in Scopus ↗   Google Scholar ↗

[7]   S.F. Ahmed, M. Khalid, W. Rashmi, A. Chan, K.J.R. Shahbaz, S.E. Reviews
Recent Progress in Solar Thermal Energy Storage Using Nanomaterials, vol. 67 (2017), pp. 450-460

[PDF] View PDF   View article   View in Scopus ↗   Google Scholar ↗

[8]   K. Pillai, B. Brinkworth
The storage of low grade thermal energy using phase change materials
Appl. Energy, 2 (3) (1976), pp. 205-216

[PDF] View PDF   View article   View in Scopus ↗   Google Scholar ↗

[9]   A. Abhat
Low temperature latent heat thermal energy storage: heat storage materials
Sol. Energy, 30 (4) (1983), pp. 313-332

[PDF] View PDF   View article   View in Scopus ↗   Google Scholar ↗

[10]   T.-C. Ling, C.-S. Poon
Use of phase change materials for thermal energy storage in concrete: an overview
Constr. Build. Mater., 46 (2013), pp. 55-62

[PDF] View PDF   View article   View in Scopus ↗   Google Scholar ↗

[11]   M.F. Demirbas

Thermal energy storage and phase change materials: an overview

Energy Sources B Energy Econ. Plann., 1 (1) (2006), pp. 85-95

Crossref ↗   Google Scholar ↗

[12]   A. Elgafy, K.J.C. Lafdi

Effect of carbon nanofiber additives on thermal behavior of phase change materials

43 (15) (2005), pp. 3067-3074

[PDF] View PDF   View article   View in Scopus ↗   Google Scholar ↗

[13]   W. Yu, H.J. J.o. n. Xie

A Review on Nanofluids: Preparation, Stability Mechanisms, and Applications, vol. 2012 (2012), pp. 1-17

Crossref ↗   Google Scholar ↗

[14]   W. Yu, D.M. France, J.L. Routbort, S.U. Choi

Review and comparison of nanofluid thermal conductivity and heat transfer enhancements

Heat. Transf. Eng., 29 (5) (2008), pp. 432-460

Crossref ↗   View in Scopus ↗   Google Scholar ↗

[15]   V. Halté, J.-Y. Bigot, B. Palpant, M. Broyer, B. Prével, A.J.A.P.L. Pérez

Size dependence of the energy relaxation in silver nanoparticles embedded in dielectric matrices

75 (24) (1999), pp. 3799-3801

View in Scopus ↗   Google Scholar ↗

[16]   S. Parvate, J. Singh, J.R. Vennapusa, P. Dixit, S. Chattopadhyay

Copper nanoparticles interlocked phase-change microcapsules for thermal buffering in packaging application

J. Ind. Eng. Chem., 102 (2021), pp. 69-85

[PDF] View PDF   View article   View in Scopus ↗   Google Scholar ↗

[17]   D. Wu, et al.

Thermal conductivity enhancement of diatomite-based composite phase change materials by interfacial reduction deposition of Cu nanoparticles

J. Energy Storage, 61 (2023), Article 106861

View PDF   View article   View in Scopus ↗   Google Scholar ↗

[18]   A.P. Ingle, N. Duran, M. Rai

Bioactivity, mechanism of action, and cytotoxicity of copper-based nanoparticles: a review

Appl. Microbiol. Biotechnol., 98 (2014), pp. 1001-1009

Crossref ↗   View in Scopus ↗   Google Scholar ↗

[19]   Y.-R. Huang, P.-H. Chuang, C.L. Chen, M. Transfer

Molecular-dynamics Calculation of the Thermal Conduction in Phase Change Materials of Graphene Paraffin Nanocomposites, vol. 91 (2015), pp. 45-51

View PDF   View article   Crossref ↗   Google Scholar ↗

[20]   S. Harish, D. Orejon, Y. Takata, M. Kohno

Thermal conductivity enhancement of lauric acid phase change nanocomposite with graphene nanoplatelets

Appl. therm. Eng., 80 (2015), pp. 205-211

View PDF   View article   View in Scopus ↗   Google Scholar ↗

[21]   R. Ghasemiasl, S. Hoseinzadeh, M.A. Javadi, H. Transfer

Numerical analysis of energy storage systems using two phase-change materials with nanoparticles

J. Thermophys. Heat Tran., 32 (2) (2018), pp. 440-448

Crossref ↗   View in Scopus ↗   Google Scholar ↗

[22]   Y. Huo, Z.J.E.C. Rao, Management

Lattice Boltzmann Investigation on Phase Change of Nanoparticle-Enhanced Phase Change Material in a Cavity with Separate Plate, vol. 154 (2017), pp. 420-429

View PDF   View article   View in Scopus ↗   Google Scholar ↗

[23]   Y.-M. Chu, D. Yadav, A. Shafee, Z. Li, Q.-V. Bach

Influence of Wavy Enclosure and Nanoparticles on Heat Release Rate of PCM Considering Numerical Study, vol. 319 (2020), Article 114121

View PDF   View article   View in Scopus ↗   Google Scholar ↗

[24]   M. Hekmatifar, D. Toghraie, B. Mehmandoust, F. Aghadavoudi, S.A. Eftekhari, M. Transfer

Molecular Dynamics Simulation of the Phase Transition Process in the Atomic Scale for Ar/Cu Nanofluid on the Platinum Plates, vol. 117 (2020), Article 104798

View PDF   View article   View in Scopus ↗   Google Scholar ↗

[25]   R. Martínez-García, et al.

The present state of the use of waste wood ash as an eco-efficient construction material: a review

Materials, 15 (15) (2022), p. 5349

Crossref ↗   View in Scopus ↗   Google Scholar ↗

[26]   A.İ. Çelik, *et al.*

Mechanical behavior of crushed waste glass as replacement of aggregates

Materials, 15 (22) (2022), p. 8093

Crossref ↗   View in Scopus ↗   Google Scholar ↗

[27]   S. Yaghoubi, B. Rezaye, S.M. Sajadi, M. Shahgholi, M. Inc

Developed molecular dynamics method of dissipative particle dynamics for the bench mark numerical simulation of fluid flow inside a rectangular chamber

Eng. Anal. Bound. Elem., 149 (2023), pp. 112-126

📄 View PDF   View article   View in Scopus ↗   Google Scholar ↗

[28]   G. Kou, M. Jahanbakhsh, M. Molaee, N. Abbasi, M. Shahgholi, M. Inc

MD analysis of heat transfer of carbon nanotube flow on nanopumping process to improve the hydrodynamic and thermal performances

Eng. Anal. Bound. Elem., 144 (2022), pp. 507-517

📄 View PDF   View article   View in Scopus ↗   Google Scholar ↗

[29]   D.J. Evans, B.L. Holian

The nose–hoover thermostat

J. Chem. Phys., 83 (8) (1985), pp. 4069-4074

View in Scopus ↗   Google Scholar ↗

[30]   C. Nie, X. Tong, S. Wu, S. Gong, D.J. R.a. Peng

Paraffin confined in carbon nanotubes as nano-encapsulated phase change materials: experimental and molecular dynamics studies

5 (113) (2015), pp. 92812-92817

View in Scopus ↗   Google Scholar ↗

[31]   C. Wang, L. Gao, M. Liu, S. Xia, Y. Han

Self-crystallization behavior of paraffin and the mechanism study of SiO_2 nanoparticles affecting paraffin crystallization

Chem. Eng. J., 452 (2023), Article 139287

📄 View PDF   View article   View in Scopus ↗   Google Scholar ↗

[32]   Y. Hou, H. Chen, X. Liu

Experimental study on the effect of partial filling of copper foam on heat storage of paraffin-based PCM

Renew. Energy, 192 (2022), pp. 561-571

[PDF] View PDF   View article   View in Scopus ↗   Google Scholar ↗

[33]   J. Cao, L. Liu, C. Liu, C. He

Phase transition mechanisms of paraffin in waxy crude oil in the absence and presence of pour point depressant

J. Mol. Liq., 345 (2022), Article 116989

[PDF] View PDF   View article   View in Scopus ↗   Google Scholar ↗

[34]   N. Putra, E. Prawiro, M. Amin

Thermal properties of beeswax/CuO nano phase-change material used for thermal energy storage

Int .J. Technol., 7 (2) (2016), pp. 244-253

Crossref ↗   View in Scopus ↗   Google Scholar ↗

[35]   J. Wang, H. Xie, Z. Guo, L. Guan, Y. Li

Improved thermal properties of paraffin wax by the addition of TiO2 nanoparticles

Appl. Therm. Eng., 73 (2) (2014), pp. 1541-1547

[PDF] View PDF   View article   View in Scopus ↗   Google Scholar ↗

[36]   B.J. Alder, T.E. Wainwright

Studies in molecular dynamics. I. General method

J. Chem. Phys., 31 (2) (1959), pp. 459-466

Crossref ↗   View in Scopus ↗   Google Scholar ↗

[37]   D.C. Rapaport, D.C.R. Rapaport

The Art of Molecular Dynamics Simulation

Cambridge university press (2004)

Google Scholar ↗

[38]   Q. Spreiter, M. Walter

Classical molecular dynamics simulation with the Velocity Verlet algorithm at strong external magnetic fields

J. Comput. Phys., 152 (1) (1999), pp. 102-119

[PDF] View PDF   View article   View in Scopus ↗   Google Scholar ↗

[39]   E. Hairer, C. Lubich, G. Wanner

Geometric numerical integration illustrated by the Störmer–Verlet method

Acta Numer., 12 (2003), pp. 399-450

View in Scopus ↗   Google Scholar ↗

[40]   D. Toghraie, M. Hekmatifar, Y. Salehipour, M. Afrand

Molecular dynamics simulation of Couette and Poiseuille Water-Copper nanofluid flows in rough and smooth nanochannels with different roughness configurations

Chem. Phys., 527 (2019), Article 110505

📄 View PDF   View article   View in Scopus ↗   Google Scholar ↗

[41]   M.S. Daw, M.I. Baskes

Embedded-atom method: derivation and application to impurities, surfaces, and other defects in metals

Phys. Rev. B, 29 (12) (1984), p. 6443

View in Scopus ↗   Google Scholar ↗

[42]   J.E. Lennard-Jones

Cohesion

Proc. Phys. Soc., 43 (5) (1931), p. 461

1926-1948)

View in Scopus ↗   Google Scholar ↗

[43]   E.S. Toberer, M. Christensen, B. Iversen, G.J. Snyder

High temperature thermoelectric efficiency in Ba 8 Ga 16 Ge 30

Phys. Rev. B, 77 (7) (2008), Article 075203

Crossref ↗   View in Scopus ↗   Google Scholar ↗

[44]   J.E. Lennard-Jones

Cohesion

Proc. Phys. Soc., 43 (5) (1931), p. 461

View in Scopus ↗   Google Scholar ↗

[45]   A.K. Rappé, C.J. Casewit, K. Colwell, W.A. Goddard III, W.M. Skiff

UFF, a full periodic table force field for molecular mechanics and molecular dynamics simulations

J. Am. Chem. Soc., 114 (25) (1992), pp. 10024-10035

Crossref ↗   View in Scopus ↗   Google Scholar ↗

[46]   S.L. Mayo, B.D. Olafson, W.A. Goddard

DREIDING: a generic force field for molecular simulations

J. Phys. Chem., 94 (26) (1990), pp. 8897-8909

Crossref ↗   View in Scopus ↗   Google Scholar ↗

[47]   M.S. Daw, M.I. Baskes

Embedded-atom method: derivation and application to impurities, surfaces, and other defects in metals

Phys. Rev. B, 29 (12) (1984), p. 6443

View in Scopus ↗   Google Scholar ↗

[48]   P.G. Huray

Maxwell's Equations

John Wiley & Sons (2011)

Google Scholar ↗

Cited by (0)

ELSEVIER

RELX™